Workshop on Multineutron Clusters in Nuclei and in Stars

June 2-6, 2025

Lauro TOMIO

Instituto de Física Teórica, UNESP, São Paulo, Brazil

Role of Coulomb breakup cross-sections at sub-barrier energies, with ^{11}Be projectile on heavy targets

Collaboration with

Bahati MUKERU and **Tapiwa SITHOLE**

Department of Physics, University of South Africa (UNISA)

Role of Coulomb breakup cross-sections at sub-barrier energies, with ^{11}Be projectile on heavy targets

Outline:

- Resume
- Introduction
- Theoretical and numerical approach
- Main results
- Conclusion

Resume:

Considering the total fusion and breakup cross-sections in the interaction of the neutron-halo ^{11}Be projectile on the lead target ^{208}Pb, it is shown that, even for the neutron-halo projectile, the breakup channel remains the most dominant reaction channel at sub-barrier energies.

This follows a characteristic behavior that was previously found for the proton-halo projectile ^{8}B.

This is shown to occur due to the continuum-continuum couplings coming exclusively from its Coulomb component.

The enhancement of the Coulomb breakup cross-section at sub-barrier incident energies by the continuum-continuum couplings is speculated to be associated with the projectile breaking up on the outgoing trajectory, provided these couplings can be proven to delay the breakup process.

Introduction:

A recent analysis by Yang et al. [Nature Communications 13 (2022) 7193] of the ^{8}B proton-halo nucleus reaction on a lead target at deep sub-barrier energies confirmed previous measurement of the same reaction by Pakou et al. [Phys. Rev. C 102 (2020) 031601(R)]. It has been reported that the breakup channel at these energies is the main reaction channel.

Also by analyzing the effect of Coulomb polarization on the proton halo state, one can infer that the prompt breakup mechanism occurs predominantly on the outgoing trajectory.

This corroborates a conclusion by Mukeru, Ndala and Lekala [Pramana J. Phys. 95 (2021)106] that the breakup of the projectile occurs in the outgoing trajectory.

It is being emphasized also by Yang et al. the relevance of elucidating the long-standing question of the breakup dynamics of a proton halo nucleus.

We aimed to explore an extension of previous studies on proton-halo reactions on heavy targets, by considering a neutron-halo projectile, to prove the possible universality of previous conclusions.

We consider the breakup dynamics of the s-wave neutron-halo nucleus ^{11}Be on a lead target at Coulomb sub-barrier and around-barrier incident energies.

The main goal was to verify whether, for deep sub-barrier incident energies, the breakup cross-section remains dominant over the total fusion cross-section, as it happens in the case of proton-halo projectiles.

For details, see Mukeru, Sithole, LT, J. Phys. G 51 (2024) 095103.

Brief theoretical approach

CDCC Formalism

M. Yahiro et al., "The continuum discretized coupled-channels method and its applications", Prog. Theor. Exp. Phys. 2012, 01A206

In our numerical approach, we use the CDCC (continuum discretized coupled channels) formalism. Once the total wave function is expanded on the projectile bound and bin states (whose wave functions are square-integrable), a truncated set of coupled differential equations of the radial part $\chi_\beta(R)$ of the wave function is obtained, which contains the Coupling matrix elements:

$$U_{\beta\beta'}^{LL'J}(R) = \langle \mathcal{Y}_\beta^{LJ}(\boldsymbol{r}, \boldsymbol{\Omega_R}) | U_{pt}(\boldsymbol{r}, \boldsymbol{R}) | \mathcal{Y}_{\beta'}^{L'J}(\boldsymbol{r}, \boldsymbol{\Omega_R}) \rangle,$$

where $\mathcal{Y}_\beta^{LJ}(\boldsymbol{r}, \boldsymbol{\Omega_R})$ is the channel wave function (bound and bin functions), $\Omega_{\boldsymbol{R}}$ is the solid angle in the direction of the projectile-target center-of-mass $\boldsymbol{R}$, in spherical coordinates, with L and J being the orbital and total angular momentum numbers.
$U_{pt}(\boldsymbol{r}, \boldsymbol{R}) = U_{ct}(\boldsymbol{R}_{ct}) + U_{vt}(\boldsymbol{R}_{vt})$, with U_{ct}, and U_{vt}, are core-target and valence-nucleon-target optical potentials, with

$$\boldsymbol{R}_{ct} \equiv \boldsymbol{R} + \frac{1}{A_p}\boldsymbol{r}, \quad \boldsymbol{R}_{vt} \equiv \boldsymbol{R} - \frac{A_c}{A_p}\boldsymbol{r},$$

where A_c and $A_p = A_c + 1$, are the core and projectile atomic mass numbers, respectively. $\beta \equiv (\alpha_b, \alpha_i)$, where α_b represents the quantum numbers that describe the projectile bound state, with α_i standing for the quantum numbers that describe the bin states, with $i = 1, 2, \ldots, N_b$, where N_b is the number of bins.

$$\boxed{\Psi^{JM}_{\mathbf{K}_{\beta_i}}(\mathbf{r},\mathbf{R}) = \sum_{L}\sum_{i=0}^{N_b} \frac{\chi^{LJ}_{\alpha_i}(R)}{R}\mathcal{G}^{LJ}_{\alpha_i}(\mathbf{r},\Omega_{\mathbf{R}})}$$

$\mathcal{G}^{LJ}_{\alpha_i}(\mathbf{r},\Omega_{\mathbf{R}})$ provide the coupling of the direct product of the projectile wave function $\Phi_{\alpha_i}(\mathbf{r})$ with the corresponding target angular part, given by

$$\mathcal{G}^{LJ}_{\alpha_i}(\mathbf{r},\Omega_{\mathbf{R}}) = [i^L\Phi_{\alpha_i}(\mathbf{r})\otimes Y_L(\Omega_{\mathbf{R}})]_{JM},$$

$\Phi_{\alpha_i}(\mathbf{r})$ contains the square integrable bin wave functions $\phi^{J_p}_{k_i\ell}(r)$ ($i = 1, 2, \ldots, N_b$), which are expressed by

$$\boxed{\phi^{J_p}_{k_i\ell}(r) = \sqrt{\frac{2}{\pi W_{\alpha_i}}}\int_{k_{i-1}}^{k_i} \mathrm{g}_{\alpha_i}(k)\, u^{J_p}_{k\ell}(r)dk,}$$

$$\left[-\frac{\hbar^2}{2\mu_{\mathrm{pt}}}\left(\frac{d^2}{dR^2}-\frac{L(L+1)}{R^2}\right)+U^{LJ}_{\beta_i\beta_i}(R)\right]\chi^{LJ}_{\beta_i}(R)$$

$$+\sum_{\beta_i\neq\beta_i'}U^{LL'J}_{\beta_i\beta_i'}(R)\chi^{L'J}_{\beta_i'}(R)=\left[E-\varepsilon_{\beta_i}\right]\chi^{LJ}_{\beta_i}(R),$$

$$\varepsilon_{\alpha_i}=\frac{\hbar^2}{2\mu_{\mathrm{cn}}W_{\alpha_i}}\int_{k_{i-1}}^{k_i}k^2\left|\mathrm{g}_{\alpha_i}(k)\right|^2dk.$$

$$W_{\alpha_i}=\int_{k_{i-1}}^{k_i}\mathrm{g}_{\alpha_i}(k)\,dk$$

The coupling matrix elements can be split into couplings to and from the bound-state $U^{LJ}_{\alpha_b\alpha}(R)$, and couplings among the continuum states $U^{LL'J}_{\alpha_i\alpha'_i}(R)$, given by

$$U^{LJ}_{\alpha_b\alpha_i}(R) = \langle \mathcal{Y}^{LJ}_{\alpha_b}(\boldsymbol{r},\boldsymbol{\Omega_R})|U_{pt}(\boldsymbol{r},\boldsymbol{R})|\mathcal{Y}^{L'J}_{\alpha_i}(\boldsymbol{r},\boldsymbol{\Omega_R})\rangle,$$

$$U^{LL'J}_{\alpha_i\alpha'_i}(R) = \langle \mathcal{Y}^{LJ}_{\alpha_i}(\boldsymbol{r},\boldsymbol{\Omega_R})|U_{pt}(\boldsymbol{r},\boldsymbol{R})|\mathcal{Y}^{L'J}_{\alpha'_i}(\boldsymbol{r},\boldsymbol{\Omega_R}),$$

evaluated subject to the boundary conditions in the asymptotic region ($R \to \infty$),

$$\chi_\beta(R) \overset{R\to\infty}{\rightarrow} \frac{\mathrm{i}}{2}\left[H^-_{\alpha_i}(K_{\alpha_i}R)\delta_{\alpha_b\alpha_i} - H^+_{\alpha_i}(K_{\alpha_i}R)S^J_{\beta\beta'}(K_{\beta'})\right],$$

where $H^\pm_\beta(K_\beta R)$ are Coulomb-Hankel functions, and $S^J_{\alpha_i\alpha'_i}(K_{\alpha'_i})$ are the scattering S-matrix elements, with $K_{\alpha_i} = \sqrt{\frac{2\mu_{pt}(E-\varepsilon_{\alpha_i})}{\hbar^2}}$, where $\mu_{pt} = m_0A_pA_t/(A_p + A_t)$ (m_0 is the nucleon's mass and A_t the projectile atomic mass number) is the projectile-target reduced mass, E is the incident energy, with ε_{α_i} being the bin energies.

The breakup cross-section can be directly obtained from the scattering matrix:

$$\sigma_{\mathrm{BU}} = \frac{\pi}{K_{\alpha_b}^2} \sum_{J\alpha_i L\alpha_i' L'} \frac{2J+1}{2j+1} |S^J_{\alpha_i\alpha_i'}(K_{\alpha_i'})|^2,$$

where j is the total angular momentum associated with the core-nucleon relative motion, and K_{α_b}, is the initial relative momentum, which is related to the final relative momentum K_{α_i} through the following energy conservation equation $\frac{\hbar^2 K_{\alpha_i}^2}{2\mu_{pt}} - \varepsilon_{\alpha_i} = \frac{\hbar^2 K_{\alpha_b}^2}{2\mu_{pt}} + \varepsilon_b$ (where $\varepsilon_b < 0$ is the ground-state binding energy).

The total fusion cross-section can be obtained as follows:

$$\sigma_{\mathrm{TF}} = \sum_{J=0}^{J_{max}} \sigma_{\mathrm{TF}}^{(J)}$$

$$\sigma_{\mathrm{TF}}^{(J)} = \frac{2\mu_{pt}}{\hbar^2 K_{\alpha_b}} (2J+1) \sum_{\beta\beta_i} \chi_\beta^{LJ}(R) |W_{\beta\beta'}^{LL'J}(R)| \chi_\beta^{L'J}(R),$$

where $W_{\beta\beta'}^{LL'J}(R)$ are the imaginary parts of the coupling matrix elements $V_{\beta\beta'}^{LL'J}(R)$ that contain the imaginary parts of the potential $U_{pt}(\boldsymbol{r}, \boldsymbol{R})$. Therefore, they are responsible for nuclear absorption.

Projectile-target potentials

A selection of the projectile-target potentials necessary to calculate both fusion and breakup cross-sections on the same footing can prove to be a challenging task. The main reason is the fact that both cross-sections emanate from different dynamics. Quite often in the literature, the Woods-Saxon form factor is used to model the real and imaginary parts of the potentials $U_{pt}(\boldsymbol{r}, \boldsymbol{R})$. With the coordinate definitions and $n \equiv ct, vt$,

$$\begin{aligned} U_n(\boldsymbol{R}_n) &= V_n(\boldsymbol{R}_n) + \mathrm{i}W_n(\boldsymbol{R}_n) \\ &= \frac{V_0^{(n)}}{1+\exp[(\boldsymbol{R}_n - \boldsymbol{R}_0^{(n)})/a_0^{(n)}]} \\ &+ \frac{\mathrm{i}\, W_0^{(n)}}{1+\exp[(\boldsymbol{R}_n - R_w^{(n)})/a_w^{(n)}]}, \quad n \equiv ct, vt \end{aligned}$$

where $V_0^{(n)}$ and $W_0^{(n)}$ are the depths of the real and imaginary parts, respectively, $R_0^{(n)} = r_0^{(n)}(A_n^{1/3} + A_t^{1/3})$ and $R_w^{(n)} = r_w^{(n)}(A_n^{1/3} + A_t^{1/3})$ are the corresponding nuclear radii, with a_{0n} and a_{wn} the respective diffuseness.

The potentials are used in the off-diagonal channels to couple bound to continuum and continuum to continuum channels. In the elastic scattering channel, the real and imaginary parts of the optical potential represent the expected value of $U_{pt}(\boldsymbol{r}, \boldsymbol{R})$, concerning the ground state of the projectile nucleus:

$$
\begin{aligned}
V_{\alpha_b\alpha_b}(\boldsymbol{R}) &= \int d^3\boldsymbol{r}|\phi_{\alpha_b}(\boldsymbol{r})|^2 V_{pt}(\boldsymbol{r}, \boldsymbol{R}), \\
W_{\alpha_b\alpha_b}(\boldsymbol{R}) &= \int d^3\boldsymbol{r}|\phi_{\alpha_b}(\boldsymbol{r})|^2 W_{pt}(\boldsymbol{r}, \boldsymbol{R}),
\end{aligned}
$$

where $\phi_{\alpha_b}(\boldsymbol{r})$ is the ground state and $V_{pt}(\boldsymbol{r}, \boldsymbol{R}) = V_{ct}(\boldsymbol{R}_{ct}) + V_{vt}(\boldsymbol{R}_{vt})$, $W_{pt}(\boldsymbol{r}, \boldsymbol{R}) = W_{ct}(\boldsymbol{R}_{ct}) + W_{vt}(\boldsymbol{R}_{vt})$, are the real and imaginary parts of $U_{pt}(\boldsymbol{r}, \boldsymbol{R})$. Given the longer tail of the projectile nucleus, due to its low breakup threshold, the nuclear forces are extended well beyond the barrier radius through the tails of $V_{pt}(\boldsymbol{r}, \boldsymbol{R})$ and $W_{pt}(\boldsymbol{r}, \boldsymbol{R})$. As such, $V_{\alpha_b\alpha_b}(\boldsymbol{R})$ will result in lowering the Coulomb barrier, whereas $W_{\alpha_b\alpha_b}(\boldsymbol{R})$ will exhibit a long-range absorption behavior. Consequently, the total fusion obtained with these potentials is expected to be much larger.

Details on the numerical calculation and parameters:

The neutron-halo projectile nucleus ^{11}Be is modeled as a ^{10}Be core nucleus to which a valence neutron is weakly bound in the $s-$wave configuration $^{10}\mathrm{Be} \otimes n(2s_{\frac{1}{2}^+})$, with $\ell_0 = 0$, where ℓ_0 is the ground-state orbital angular momentum associated with the core-neutron relative motion. The binding energy of this ground state is $\varepsilon_0 = -0.504\,\mathrm{MeV}$.
This nucleus also has an excited bound-state $\varepsilon_1 = -0.183$ MeV in the $p_{\frac{1}{2}^-}$ state ($\ell_0 = 1$), and a narrow resonance $\varepsilon_{res} = 1.274\,\mathrm{MeV}$, in the $d_{\frac{5}{2}^+}$ continuum state.

For more details, see

Mukeru et al, J. Phys. G 51 (2024) 095103 [arxiv2407.12129v1]

“Breakup dynamics of a neutron-halo projectile on heavy target at sub-barrier energies”.

We take from Capel et al. [PRC68 (2003)014612] the parameters for the real and imaginary parts of the core-target optical potential parameters used in the construction of the projectile-target coupling matrix elements:
$V_0 = 70\,\mathrm{MeV}$, $R_0 = 7.43\,\mathrm{MeV}$, $a_0 = 1.04\,\mathrm{MeV}$, $W_0 = 58.9\,\mathrm{MeV}$, $R_w = 7.19\,\mathrm{MeV}$, and $a_w = 1.0\,\mathrm{MeV}$. For the neutron-target optical potential, we adopt the global parametrization of Becchetti(1969). These potentials, together with the folding potential, in the elastic scattering channel, extend the absorption to outside the usual region, increasing the fusion cross-section. So, we need to be mindful of the choice of imaginary potentials in the analysis of the results.

To obtain fusion cross-sections comparable with the available experimental data and test how the total fusion-cross section is overestimated by the long-range imaginary potentials, we will perform another set of calculations where we replace the long-range W_{ct}, W_{nt} and W_{pt} by the short-range ones, i.e., $W_0 = 50\,\mathrm{Mev}$, $r_w = 1.0\,\mathrm{MeV}$ and $a_W = 0.1\,\mathrm{MeV}$. However, by calculating with long- or short-range imaginary potential, our interest is to verify whether the breakup cross-section remains larger than the fusion cross-section at incident energies below the Coulomb barrier.

For solving the coupled differential equations emanating from the projectile-target three-body Schrödinger equation, various numerical parameters were optimized to satisfy the convergence requirements, with the following maximum limiting applied: For the core-neutron, the orbital angular momentum ℓ was truncated at $\ell_{max} = 6\hbar$, with $r_{max} = 100\,\text{fm}$ being the maximum radial coordinate r, and $\varepsilon_{max} = 8\,\text{MeV}$ the maximum excitation energies ε. For the projectile target, we have $L_{max} = 1000\hbar$ and $R_{max} = 500\,\text{fm}$, respectively, for the maximum orbital angular momentum L and for the radial coordinate R. Also, the radial coordinates r_{max} and R_{max} were sliced into radial mesh points equally spaced by $\Delta r = 0.1\,\text{fm}$ and $\Delta R = 0.05\,\text{fm}$, respectively. The projectile-target potentials were expanded into potential multipoles up to $\lambda_{max} = 4$. The energy interval $[0, \varepsilon_{max}]$ was discretized into energy bins of widths, $\Delta\varepsilon = 0.5\,\text{MeV}$, for the s- and p-states; $\Delta\varepsilon = 1.0\,\text{MeV}$, for the f- and d-states; $\Delta\varepsilon = 1.5\,\text{MeV}$, for g-states; and $\Delta\varepsilon = 2.0\,\text{MeV}$, for higher partial waves. Finer bins were considered for the resonant state. The numerical calculations were performed with FRESCO computer codes [24]. In Fig.1, we have samples of convergence tests in terms of ℓ_{max} and ε_{max} for $E_{cm}/V_{\text{B}} = 0.8$, where $V_{\text{B}} = 37.90\,\text{MeV}$ is obtained from the São Paulo potential (SPP) [34]. As one can verify from the given results in this figure, the convergence is well reached for $\varepsilon_{max} = 8\,\text{MeV}$, and $\ell_{max} = 6\hbar$.

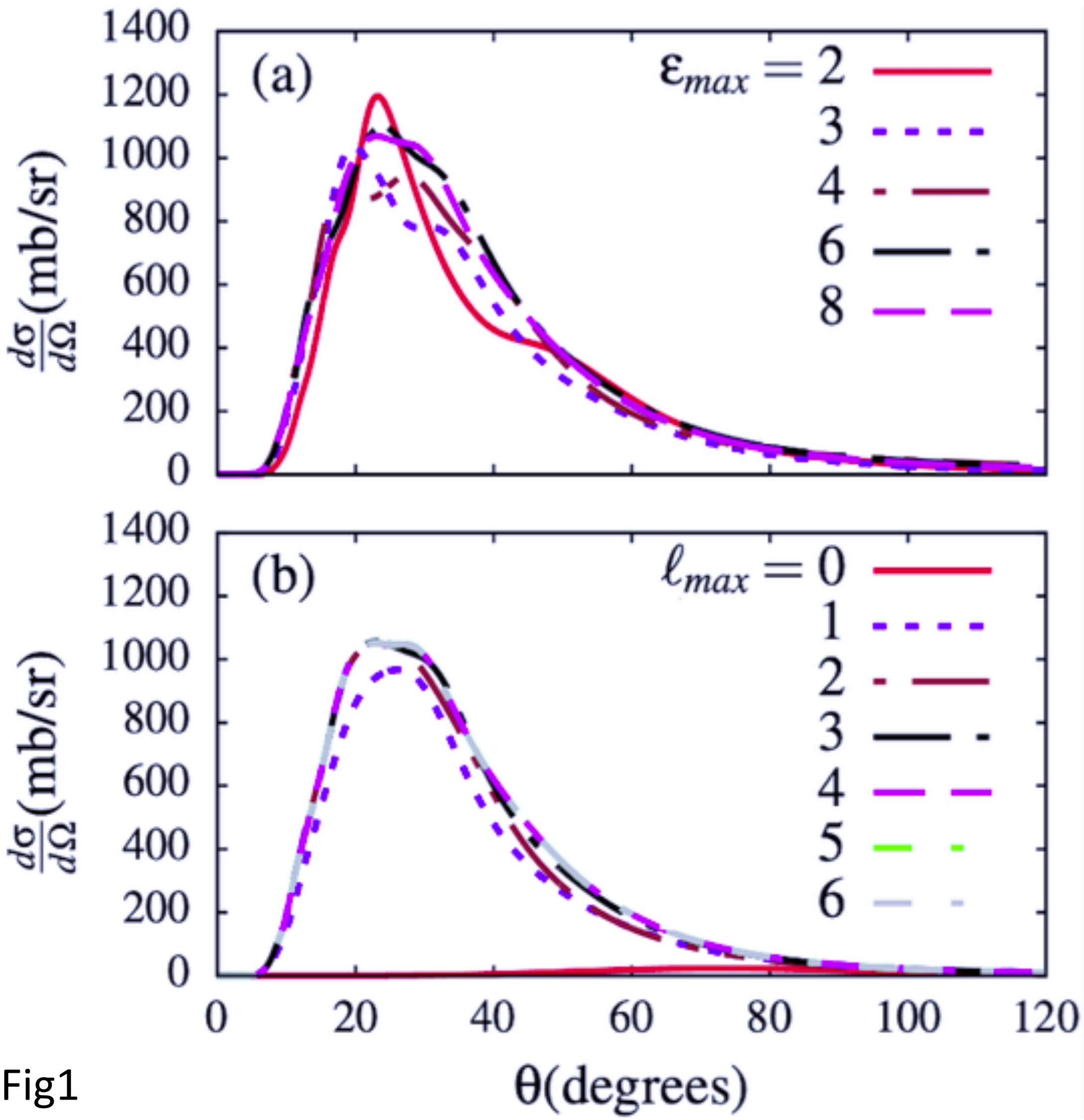

Fig1

Convergence results for the differential breakup cross-sections in terms of the maximum core-neutron excitation energies ε_{max} (MeV units) [panel (a)] and maximum core-neutron orbital angular momentum ℓ_{max} ($\hbar$ units) [panel (b)].

MAIN RESULTS AND DISCUSSION

How well our numerical results can describe experimental data is shown in Fig.2, for the differential breakup cross-section measured at $E_{lab} = 140\,\mathrm{MeV}$.

As one can find out, the breakup cross-section with the short-range imaginary potential becomes highly oscillatory, particularly at small angles, and does not provide a good fit for the experimental data as the ones obtained with the long-range imaginary potential. So, we chose to use the long-range imaginary potential to calculate the breakup cross-sections.

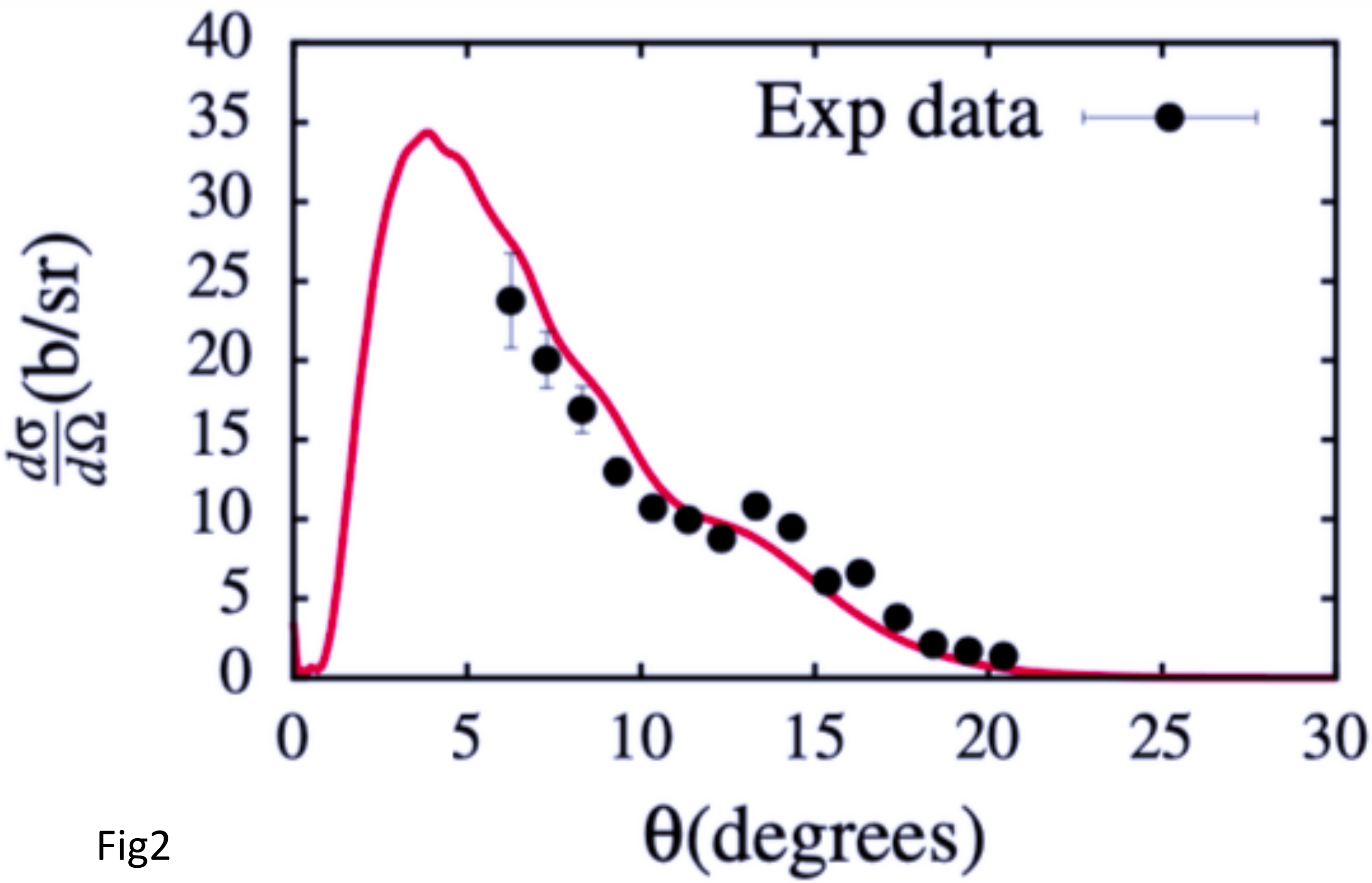

Fig2

Comparison of the theoretical computed breakup cross-section (solid line) with the corresponding experimental data, measured at $E_{lab} = 140$ MeV [Duan et al., PLB 811 (2020) 135942]

Fig.3 shows σ_{BU} and σ_{TF}, as functions of the ratio between total energy E_{cm} and potential barrier height V_B, with E_{cm}/V_{B} in the interval $[0.5, 1.3]$. The same potential parameters were applied in both calculations to obtain the breakup cross-section in Fig.2.

Although these parameters increase σ_{TF}, both fusion and breakup cross-sections are treated on the same footing, with the outcome not affected by different calculations. These results were obtained with all the different couplings being included in the coupling matrix elements, with couplings to and from the projectile bound-state and continuum-continuum couplings.

One observes that at sub-barrier energies ($E_{cm}/V_{\mathrm{B}} \leq 1$),$\sigma_{\mathrm{BU}}$ is dominant over σ_{TF}. The transition occurs around the Coulomb barrier where σ_{TF} prevails. Therefore, one can infer that, even in the case of a neutron-halo weakly-bound projectile, the breakup channel remains the dominant reaction channel at sub-barrier incident energies.

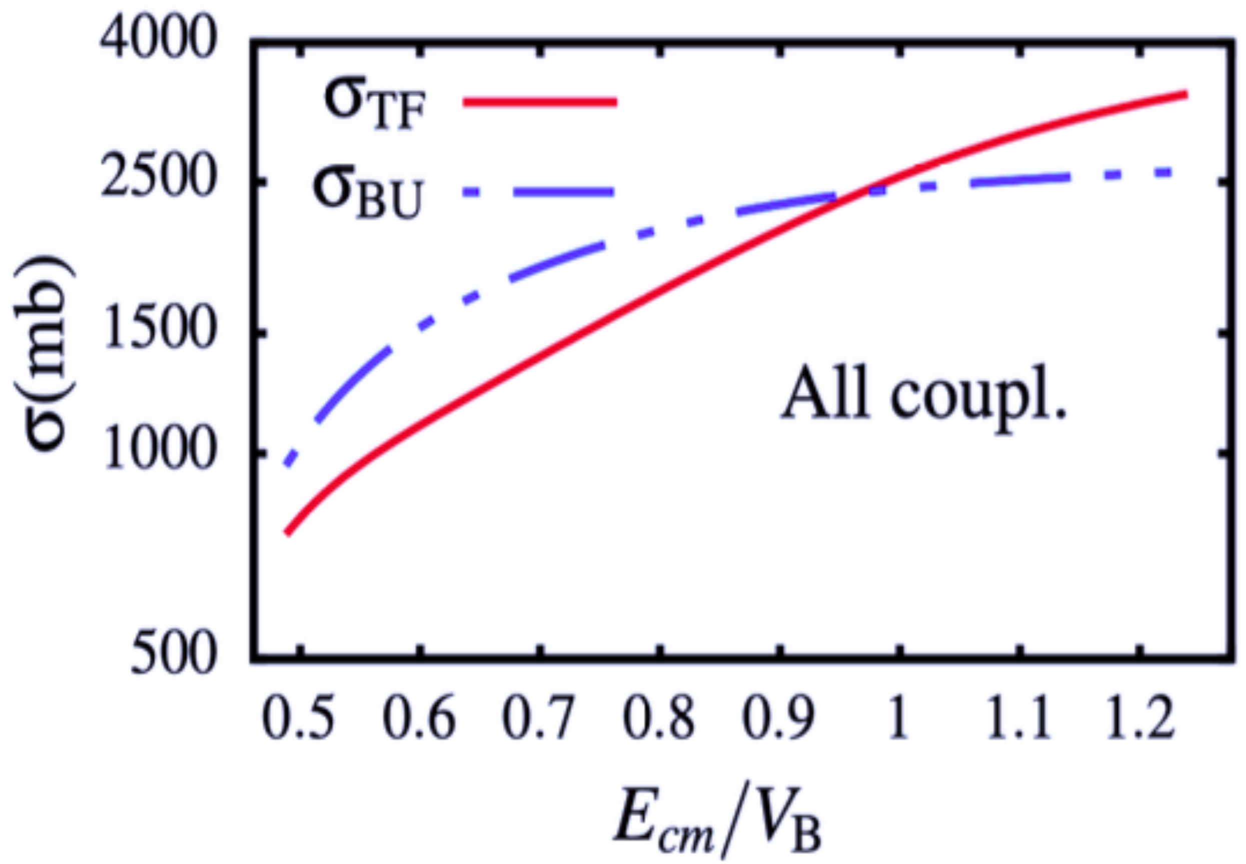

Fig3

Breakup (dash-dotted) and total fusion (solid line) cross-sections, as functions of the incident energy scaled by the Coulomb barrier height V_B, with all different coupled channels are included in the coupling matrix elements.

It is interesting to see that even when long-range imaginary potentials are considered, which are known to increase the fusion cross-section, the breakup cross-section remains more important than its fusion counterpart, following previous conclusions on proton-halo projectile.

We do not expect the use of short-range imaginary potentials to reverse this trend at sub-barrier energies, but such potentials can be expected to push the transition point where the fusion cross-section becomes more important for larger incident energies.

These results further suggest that the Coulomb barrier in the core-proton system is not responsible for the importance of σ_{BU} over σ_{TF} at sub-barrier energies, which implies that static effects related to the projectile ground-state are not the main factors contributing to this phenomenon.

As argued in Ref. Mukeru et al. [Pramana J. Phys.95 (2021)106, this leaves dynamical effects (due to the projectile-target interaction) as one of the main factors responsible for the importance of the breakup cross-section over the total fusion cross-sections at incident sub-barrier energies.

To verify how the long-range imaginary potentials overestimate $\sigma_{\rm TF}$, we repeated the same calculations, but with the short-range imaginary potentials, with results shown in Fig.4.

By comparing with results in Fig.3, it is noticed that $\sigma_{\rm TF}$ is largely suppressed, with $\sigma_{\rm BU}$ becoming dominant. Figs.3 and 4 suggest that the difference between both breakup cross-sections is not very pronounced. However, one can verify that the results obtained with short-range imaginary potentials are significantly larger than those obtained with long-range imaginary potentials.

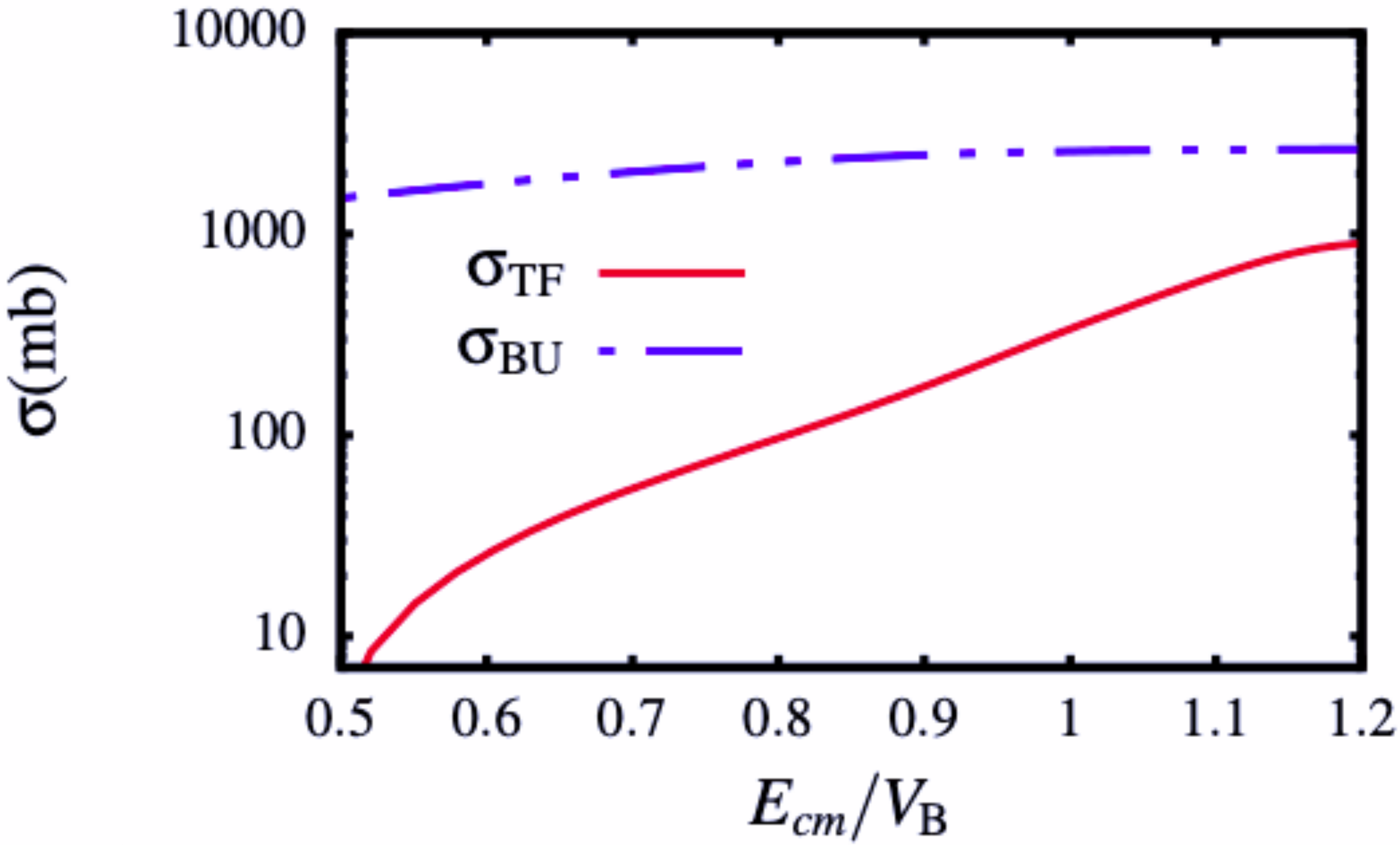

Fig4

Fusion and breakup cross-section as a function of E_{cm}/V_B, obtained when the long-range imaginary part of the nuclear potential is replaced by the short-range one, i.e., with $W_0 =$ 50 Mev, r_w = 1.0 MeV and a_w = 0.1 MeV for core-target, neutron-target and projectile-target imaginary potentials.

With Fig.5, we can see the effect of the continuum-continuum couplings, by considering when they are removed from the coupling matrix elements, i.e., leaving a single transition to and from the projectile-bound state.

A stark difference is observed from the case with all couplings: at sub-barrier energies ($E_{cm}/V_{\rm B} \leq 0.8$), both BU and TF cross-sections are almost similar. Above the Coulomb barrier, the $\sigma_{\rm BU}$ starts becoming dominant. So, the CCC appear to be responsible for the quantitative importance of $\sigma_{\rm BU}$ over $\sigma_{\rm TF}$ at sub-barrier incident energies.

However, considering the fusion calculations as given in Fig.4, with a short-range imaginary part in the nuclear potential, the $\sigma_{\rm TF}$ in the absence of the CCC would be lower than the $\sigma_{\rm BU}$ even at sub-barrier energies. So, besides not given a realistic picture, Fig.5 points out the fact that when the CCC are removed the gap between the two curves will be significantly narrowed.

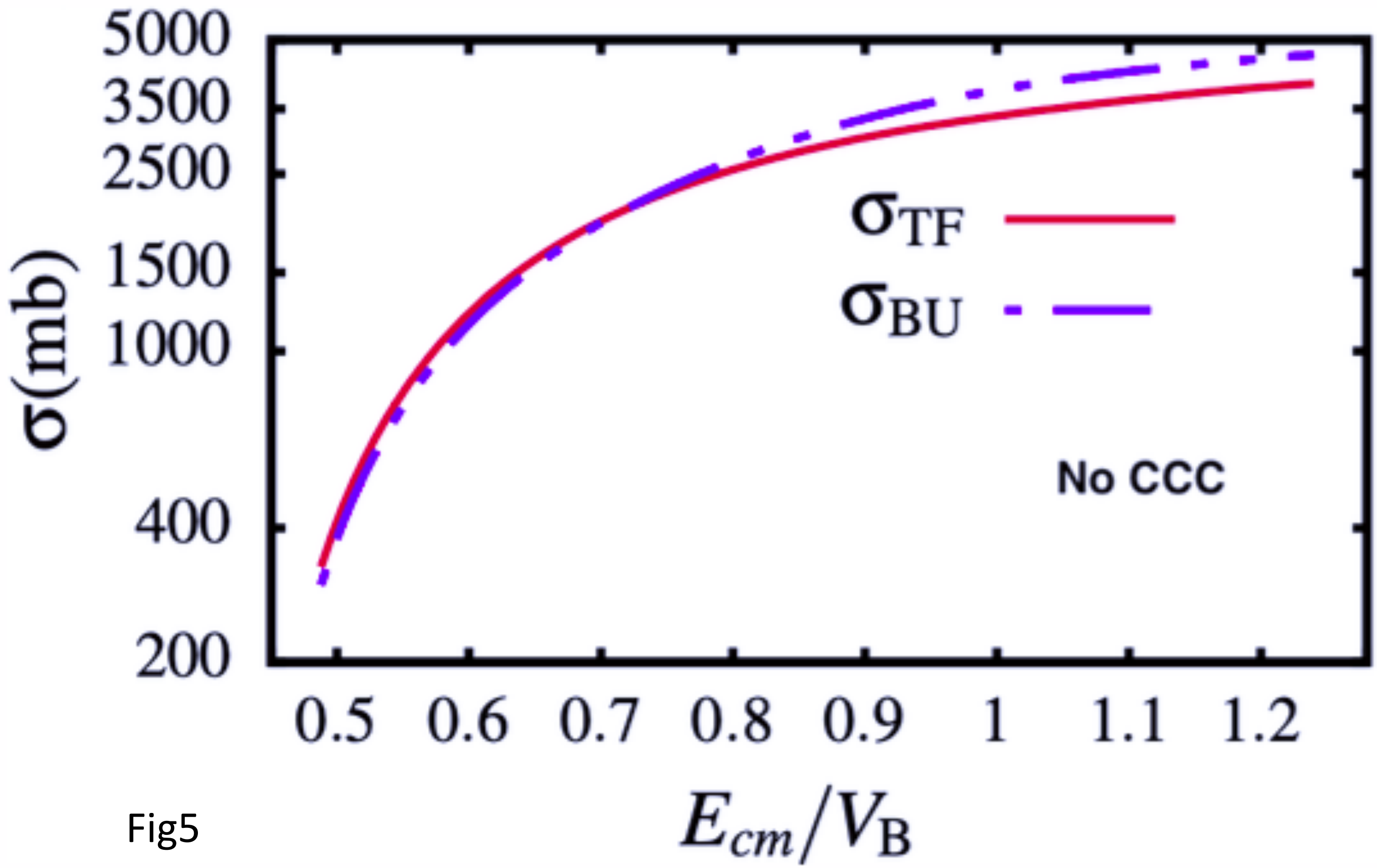

Fig5

Breakup and total fusion cross-sections as functions of the incident energy scaled by the Coulomb barrier height V_B, and obtained when the continuum-continuum couplings are excluded ("No CCC") from the coupling matrix elements.

The significance of the CCC on the σ_{BU} is also shown in Fig.6. One can notice that, at deep sub-barrier energies ($E_{cm}/V_{\mathrm{B}} \leq 0.7$), the CCC serve to enhance the σ_{BU}. σ_{BU} in the presence of these couplings is larger than in the absence of these couplings.

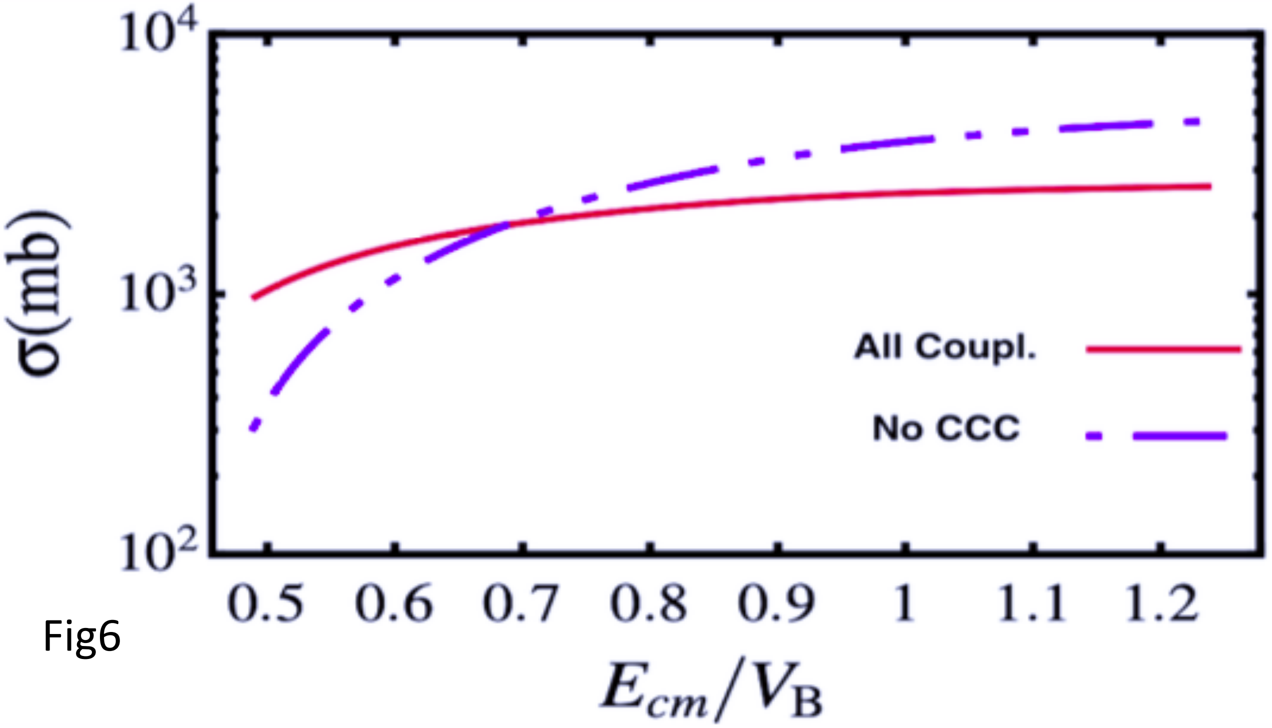

Fig6

Breakup cross-sections plotted as functions of the incident energy scaled by the Coulomb barrier height V_{B}, and obtained when all the different couplings are included in the coupling matrix elements "All coupl." and when the continuum-continuum couplings are excluded from the couplings matrix elements "No CCC".

The breakup cross-section is obtained by coherently including both Coulomb and nuclear interactions in the coupling matrix elements, which we call total (Coulomb + nuclear) breakup cross-section. The separation into its Coulomb and nuclear components is not a straightforward task. We resort on an approximate procedure. To calculate the Coulomb contribution, we removed all the core-target and neutron-target nuclear interactions from the coupling matrix elements, keeping only its monopole component in the elastic scattering channel. This potential was obtained by folding the projectile ground-state density with the projectile-target potentials. In this case, the Coulomb breakup cross-section is affected by the absorption in the elastic scattering channel due to the imaginary component of this potential. Similarly, the nuclear breakup cross-sections were obtained by removing the core-target Coulomb potential from the coupling matrix elements, also keeping its monopole diagonal term in the elastic scattering channel.

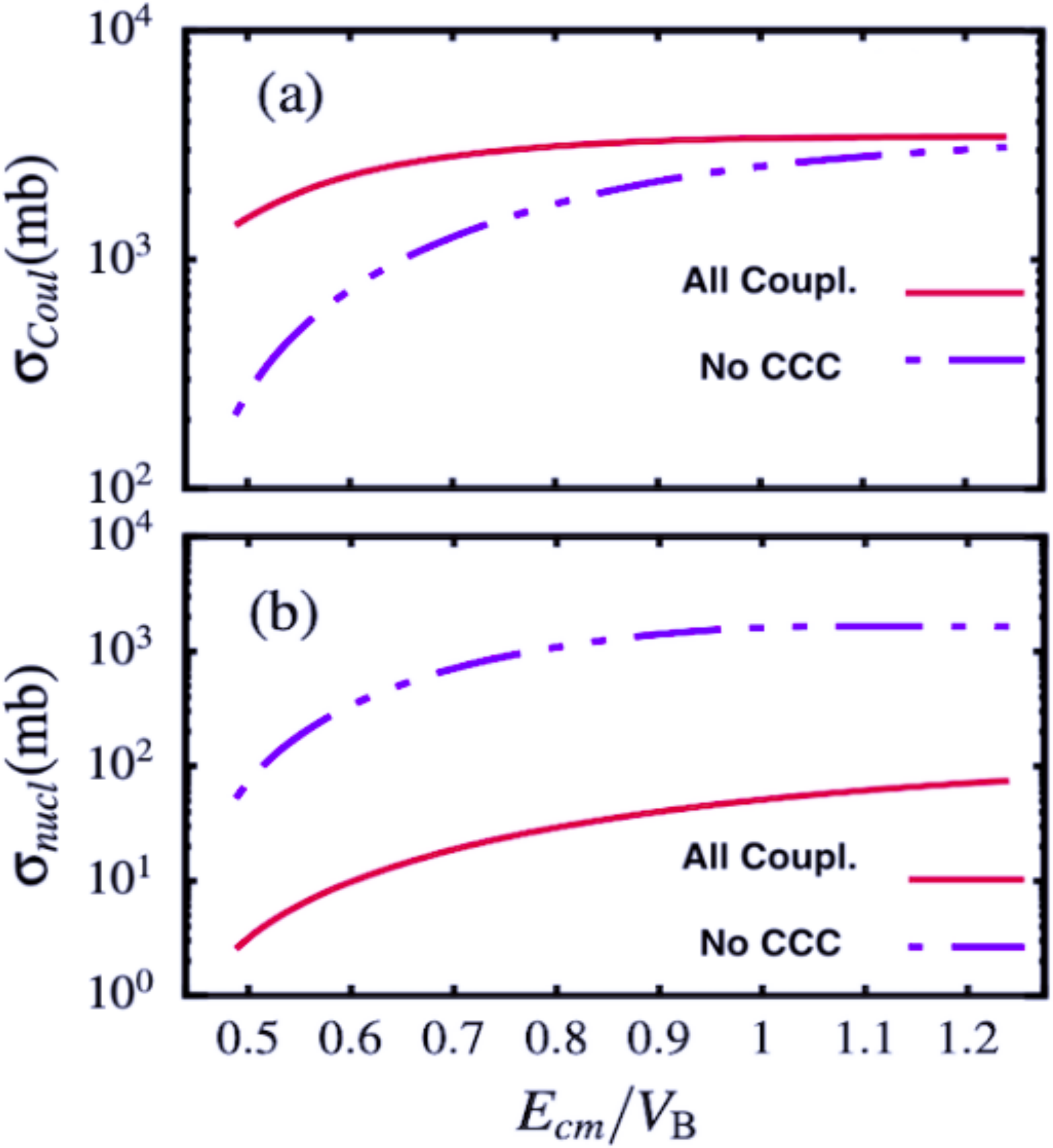

(a)
σ_{Coul}(mb)
All Coupl.
No CCC
(b)
σ_{nucl}(mb)
All Coupl.
No CCC
10^4
10^3
10^2
10^1
10^0
0.5
0.6
0.7
0.8
0.9
1
1.1
1.2
E_{cm}/V_{B}

The Coulomb and nuclear breakup cross-sections are shown in Fig.7. At sub-barrier energies, the Coulomb breakup cross-section is strongly enhanced by the continuum-continuum couplings [see panel (a)]. As the incident energy increases, the enhancement strength decreases and the trend suggests that at higher incident energies, the continuum-continuum couplings would amount to a smaller effect on the Coulomb breakup cross-section.

It has been shown that at higher incident energy, these couplings have very small suppression effect on the Coulomb breakup cross-section [Mukeru, Chin. Phys. C 46 (2022) 014103].

In contrast, panel (b) shows that the nuclear breakup cross-section is strongly suppressed by the CCC at all the displayed incident energy regions. At energies above the barrier, the nuclear breakup cross-section is known to be strongly suppressed by these couplings compared to the Coulomb breakup cross-section. In fact, this suppression is reported as one of the main reasons why the Coulomb breakup is more important than the nuclear breakup in reactions involving heavy targets. Comparing the effect of the CCC on Coulomb and nuclear breakup cross-sections, it follows that the enhancement of the total breakup cross-section at sub-barrier incident energies due to these couplings comes exclusively from the Coulomb breakup.

Conclusion

Our present study confirms the importance of the breakup channel over the total fusion channel, at energies deeply below the Coulomb barrier. As verified, previous results obtained with a proton-halo projectile on heavy targets can also be extended to the case we have a neutron-halo projectile.

Although a detailed study may be required, based on the available investigations, one can anticipate this conclusion as a universal feature in the breakup of weakly bound projectiles on heavy targets.

The enhancement of the Coulomb breakup cross-section at sub-barrier incident energies by the continuum-continuum couplings is speculated to be associated with the projectile breaking up on the outgoing trajectory, provided these couplings can be proven to delay the breakup process.

On the target mass dependence of the results

By considering lighter targets, one can verify how far the results obtained with lead can be assumed being universal.

In this direction, we have recently investigated the critical role of Coulomb interactions at sub-barrier energies, in the breakup of the ^{11}Be projectile on ^{64}Zn target, with similar results. For that, the experimental data are from Di Pietro et al., PRL 105,022701 (2010).

Preprint in preparation:

Role of Coulomb interactions at sub-barrier energies in the breakup of weakly-bound neutron-halo ^{11}Be projectile on ^{64}Zn target

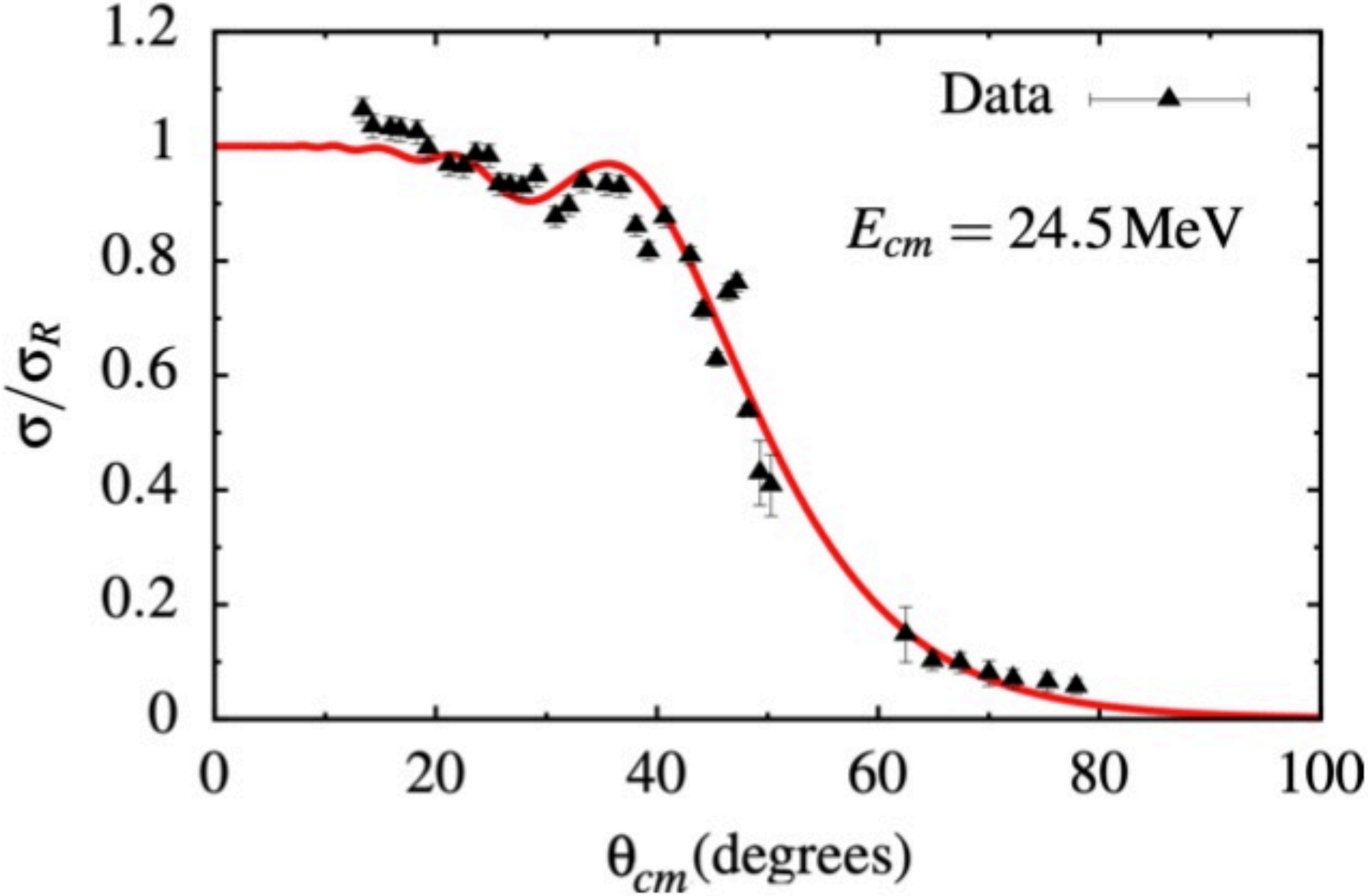

Fig. 1 Angular distribution of the ratio between elastic scattering and Rutherford cross-sections σ/σ_R, as a function of $\theta_{c.m.}$, for the ^{11}Be+^{64}Zn collision, with our numerical results (solid line) being compared with the experimental data extracted from Di Pietro et al. PRL 105, 022701 (2010), and PRC 85, 054607 (2012).

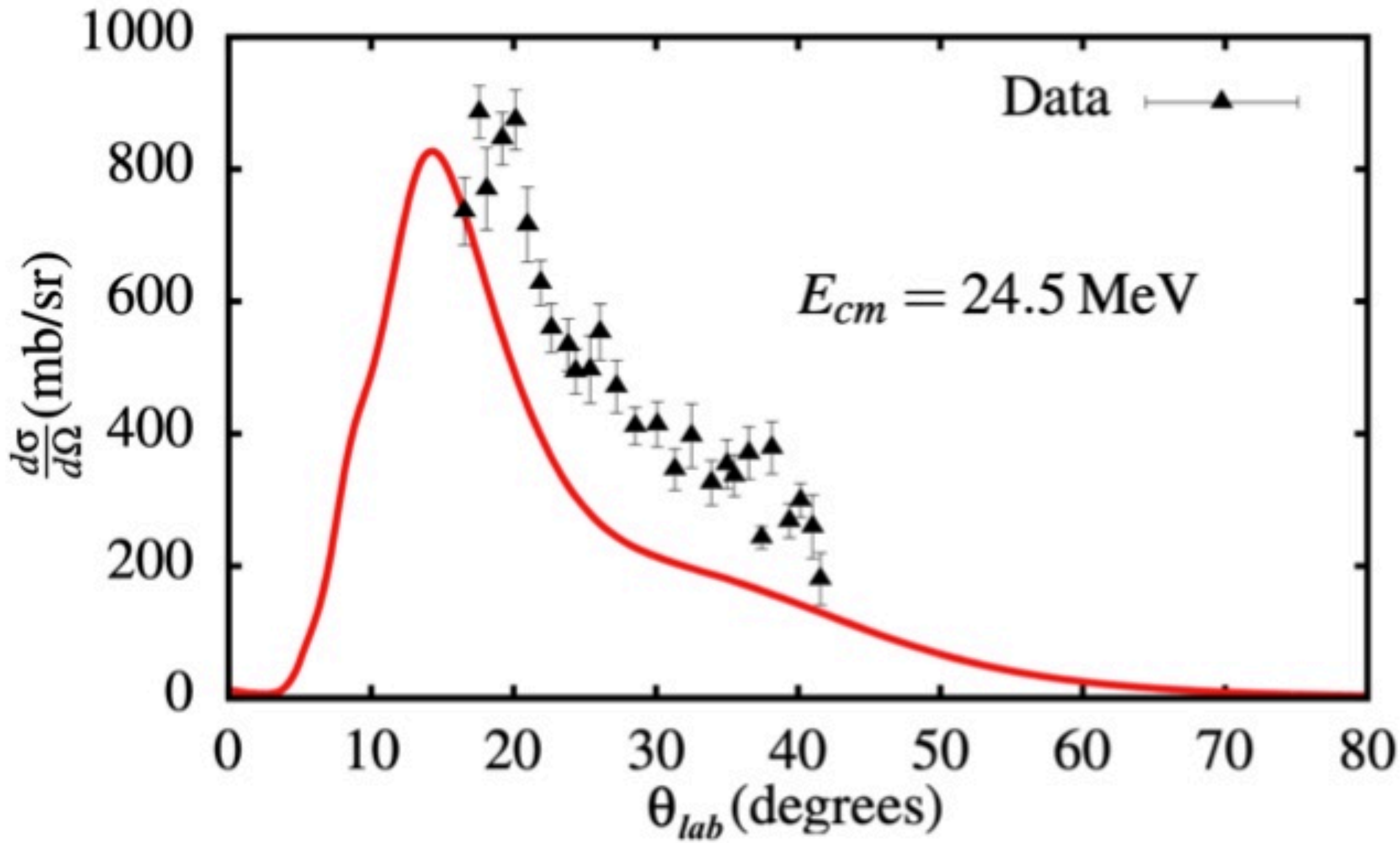

Fig. 2 **Angular distribution as a function of θ_{lab}) of the differential breakup cross-section, for the ^{11}Be+^{64}Zn collision, obtained from calculations using the unchanged neutron-target optical potential (see text for explanation), shown by the solid line. The results are compared with experimental data taken from Di Pietro et al. PRL 105, 022701 (2010).**

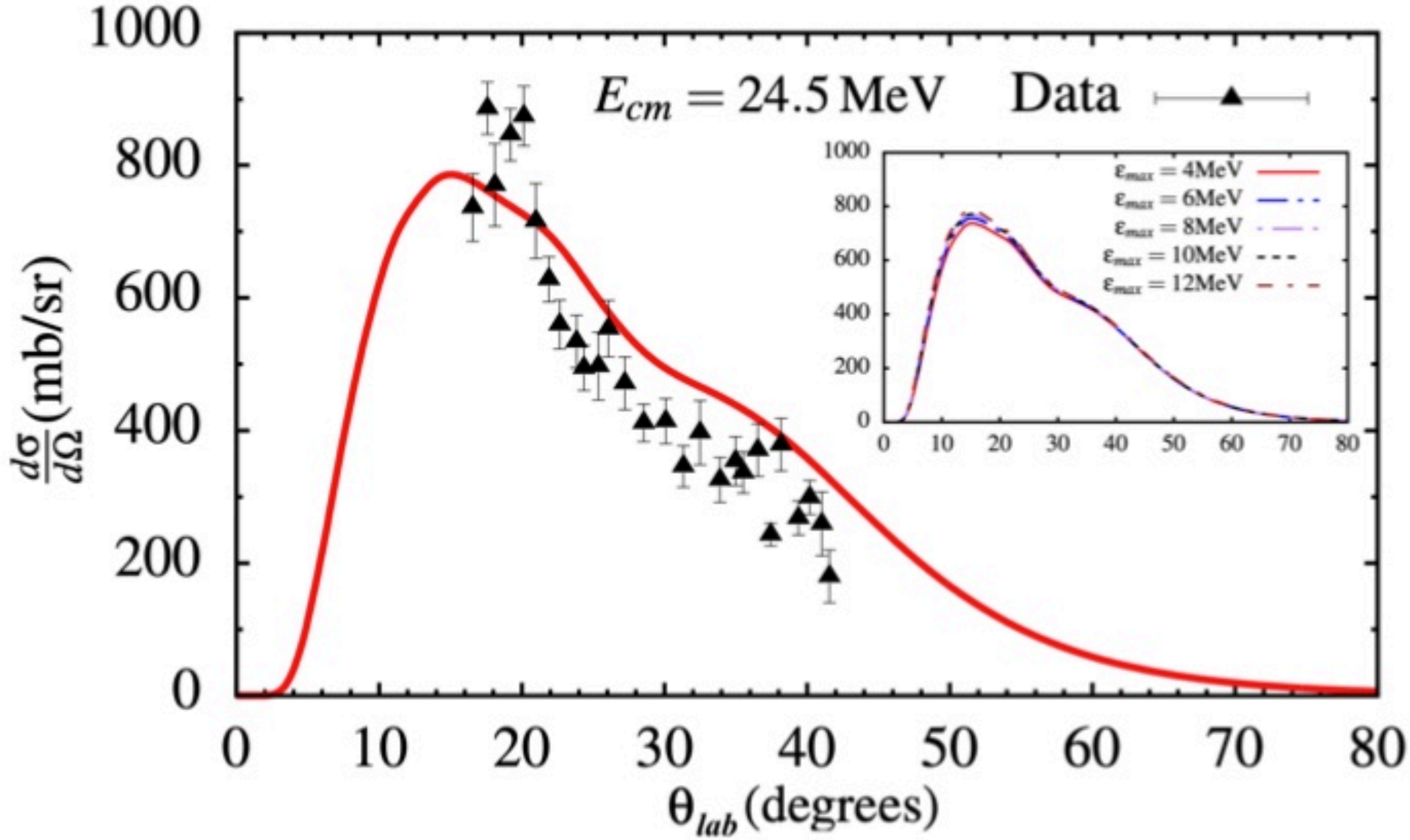

Fig. 3 Results obtained from calculations using the scaled neutron-target optical potential. The inset shows the convergence as the maximum bin excitation energy ε_{max} increases.

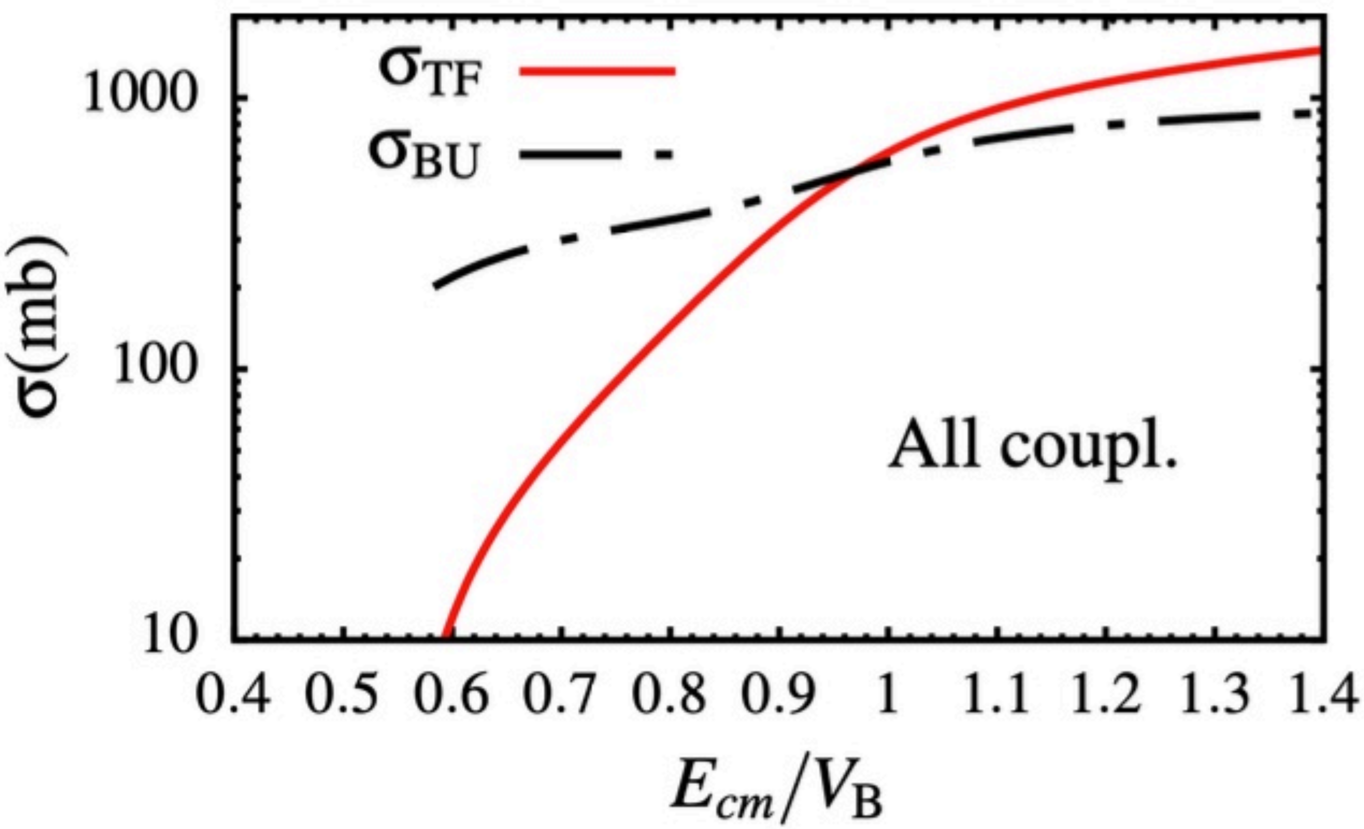

Fig. 4 Total fusion ($\sigma_{\rm TF}$) and breakup cross-sections ($\sigma_{\rm BU}$) are plotted as functions of the incident c.m. energy scaled by $V_{\rm B}$. The numerical results are obtained when all the various couplings are included in the matrix element couplings.

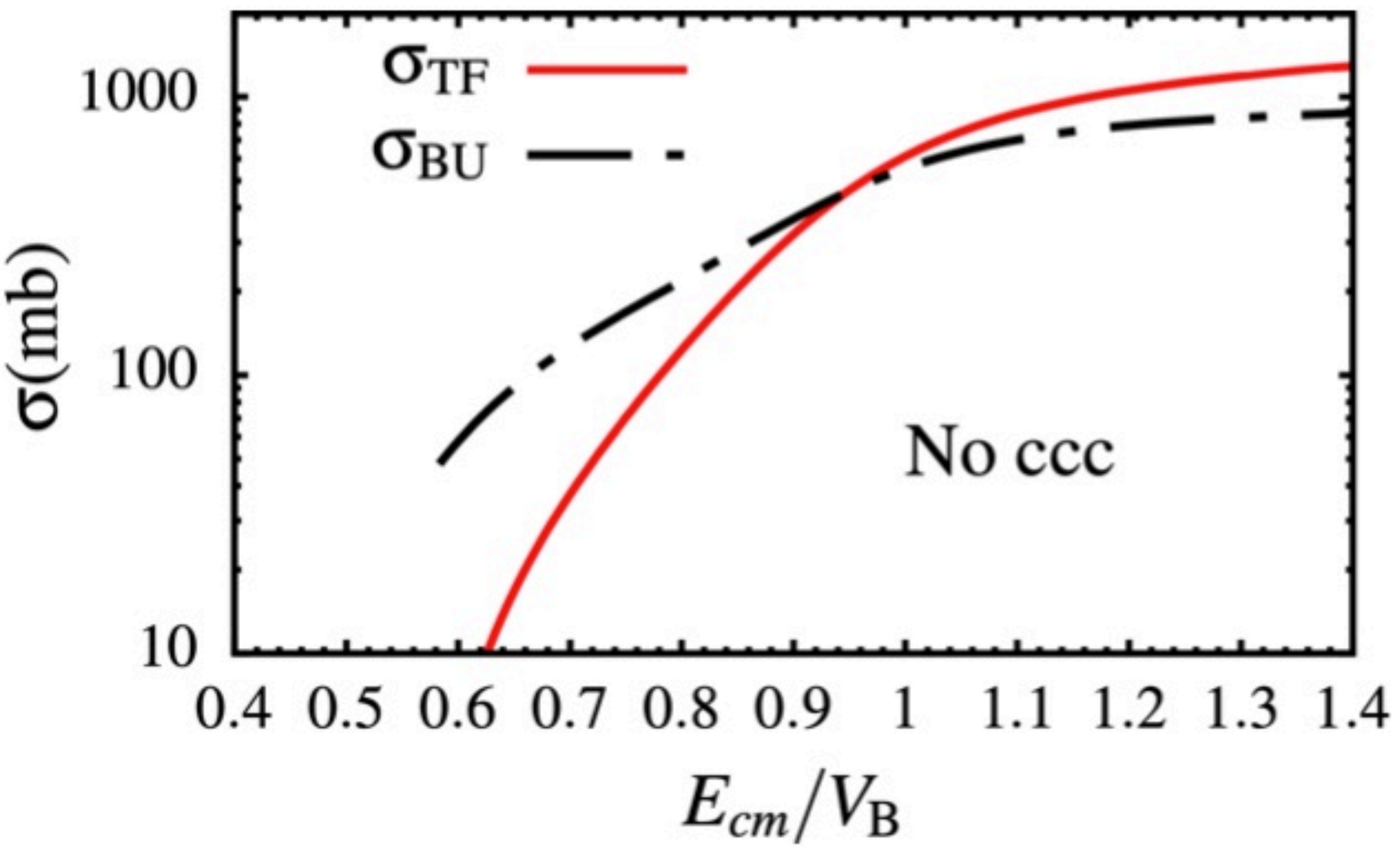

Fig. 5 **Total fusion (σ_{TF}) and breakup cross-sections (σ_{BU}) plotted as functions of the incident energy.**

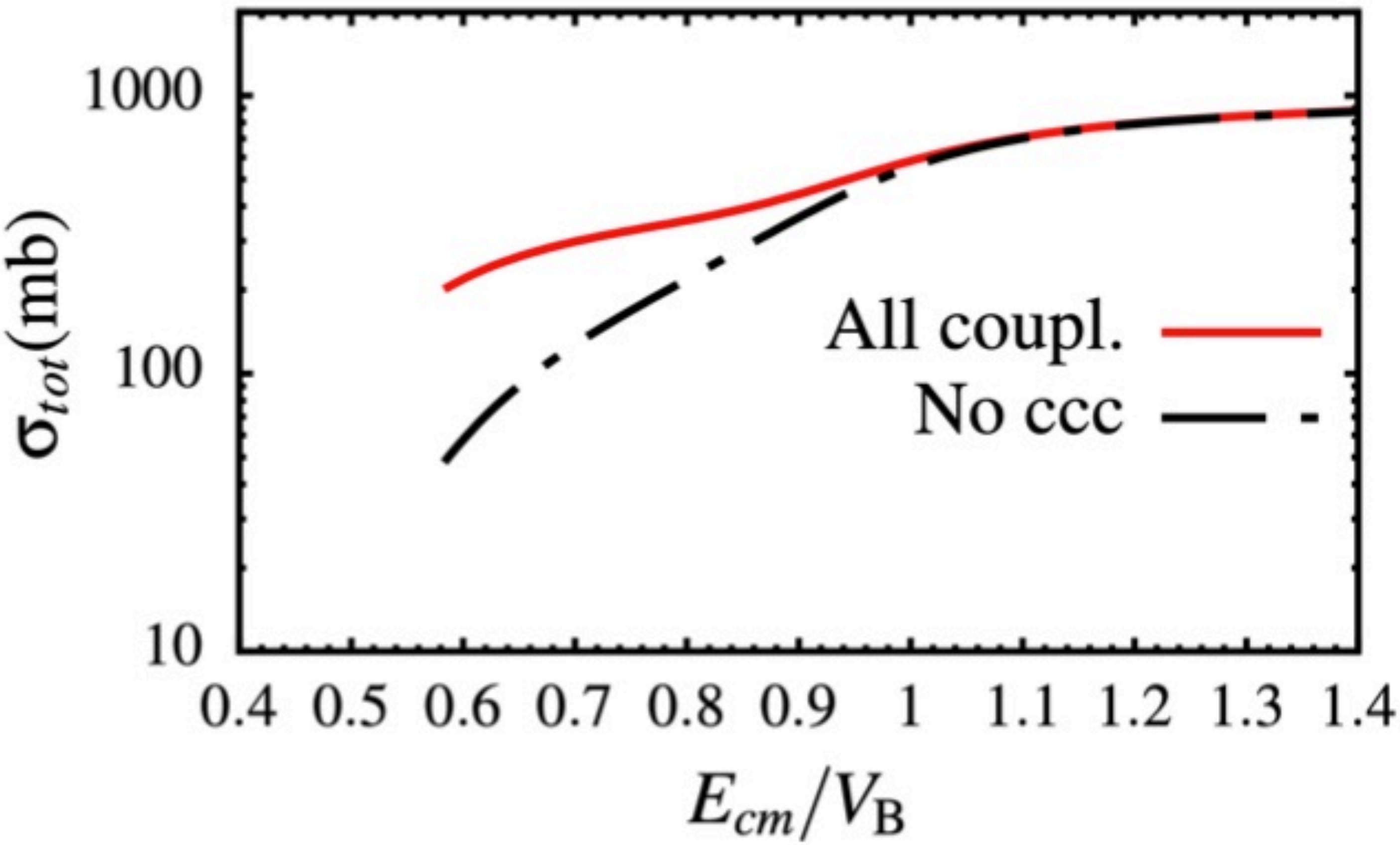

Fig. 6 Total breakup cross-sections plotted as functions of the incident energy scaled by the Coulomb barrier height V_{B}.

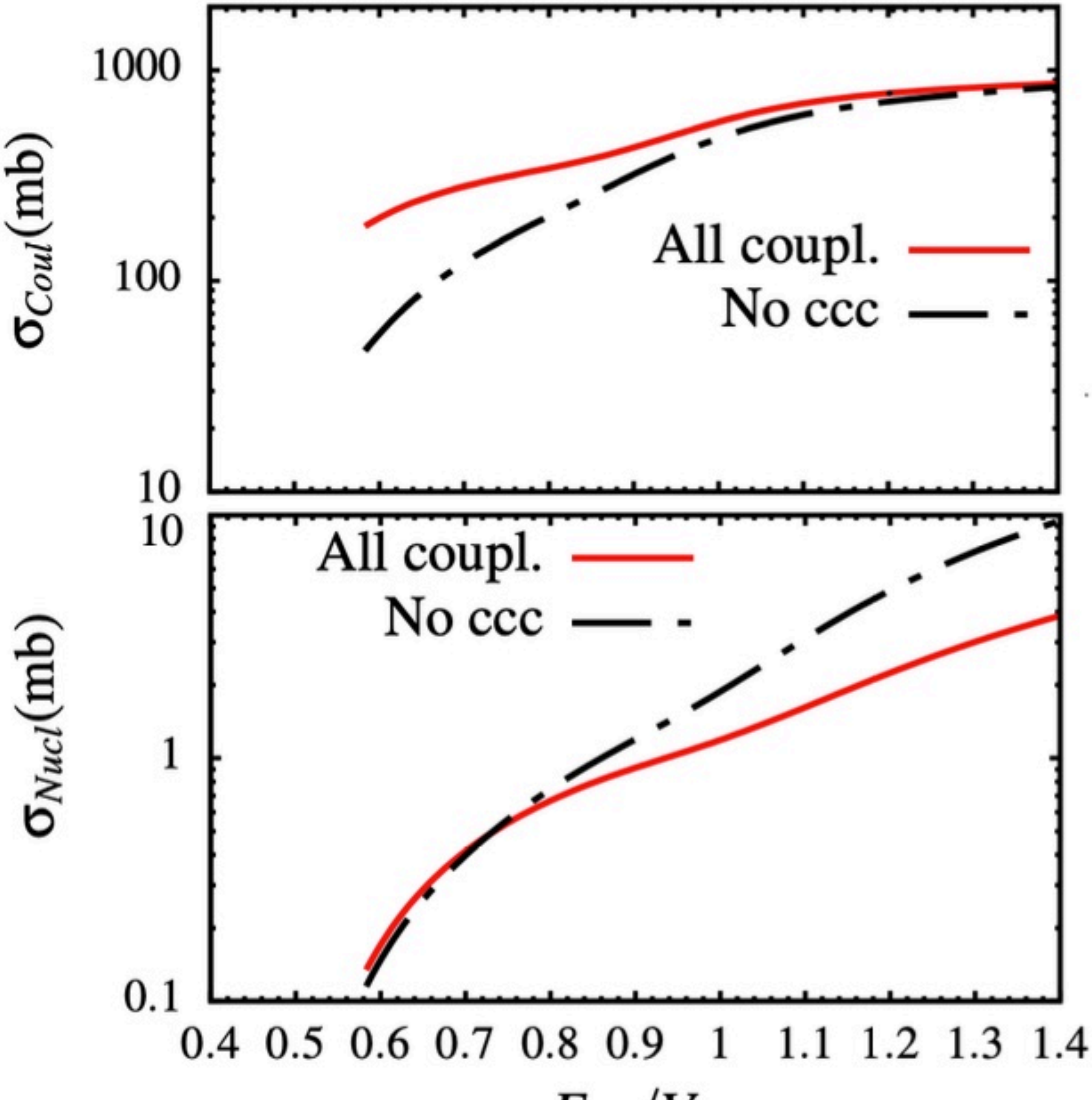

1000
100
10
σ_{Coul}(mb)
All coupl.
No ccc
10
1
0.1
σ_{Nucl}(mb)
All coupl.
No ccc
0.4 0.5 0.6 0.7 0.8 0.9 1 1.1 1.2 1.3 1.4
E_{cm}/V_{B}

The consistency of the results across different targets can provide strong experimental validation for the theoretical frameworks that predict the dominance of Coulomb breakup at sub-barrier energies.

Our results are indicating that Breakup dynamics of weakly-bound nuclei at sub-barrier energies could be predominantly governed by Coulomb interactions. Verified for two independent targets, such behavior might be independent of the target mass. However, a systematic study is needed to reach a firm conclusion in this regard, which could be a valuable theoretical insight for future studies and practical applications in nuclear physics.

THANK YOU very much for the attention!

I am also acknowledge support from CNPq (304469/2019-09)
INCT-FNA (Proc. 464898/2014-5) and FAPESP (2024/01533-7)

In our FAPESP thematic (2024/01533-7), we have available three

post-doctorate fellowships, which will be selected following our

FAPESP proposal, in

Few-Body Nuclear and Atomic Physics and Cold-Atom Physics.

Possible interested, we are inviting to apply to one of the

main researchers:

Arnaldo Gammal (IFUSP) [gammal@if.usp.br]

Airton Deppman (IFUSP) [adeppman@gmail.com]

Lauro Tomio (IFT-UNESP) [lauro.tomio@unesp.br]